JET PROPULSION LABORATORY   INTEROFFICE MEMORANDUM
CALIFORNIA INSTITUTE OF TECHNOLOGY   IOM 335N-20-01
                                                      December 16, 2020

To: Modelers and Data Analysts

From: James G. Williams and Dale H. Boggs

Subject: The JPL Lunar Laser Range Model 2020

1. Introduction

The lunar laser ranging (LLR) experiment measures the round-trip time of flight of a laser pulse fired from an observatory on the Earth, reflected from a corner-cube retroreflector array on the Moon, and received back at the observatory. We now fit 50 yr of observations stretching from 1970 to fall 2020. During those decades, the accuracy of the range measurements has improved from decimeters to millimeters. An accurate model is needed to analyze those ranges. Figure 1 shows the annual weighted rms post-fit residuals for a fit spanning 1970–2020. Figure 2 shows the annual weighted rms residuals for 1987 – March 2020. The rms residuals for 2015–2020 are 1.0 to 1.1 cm.
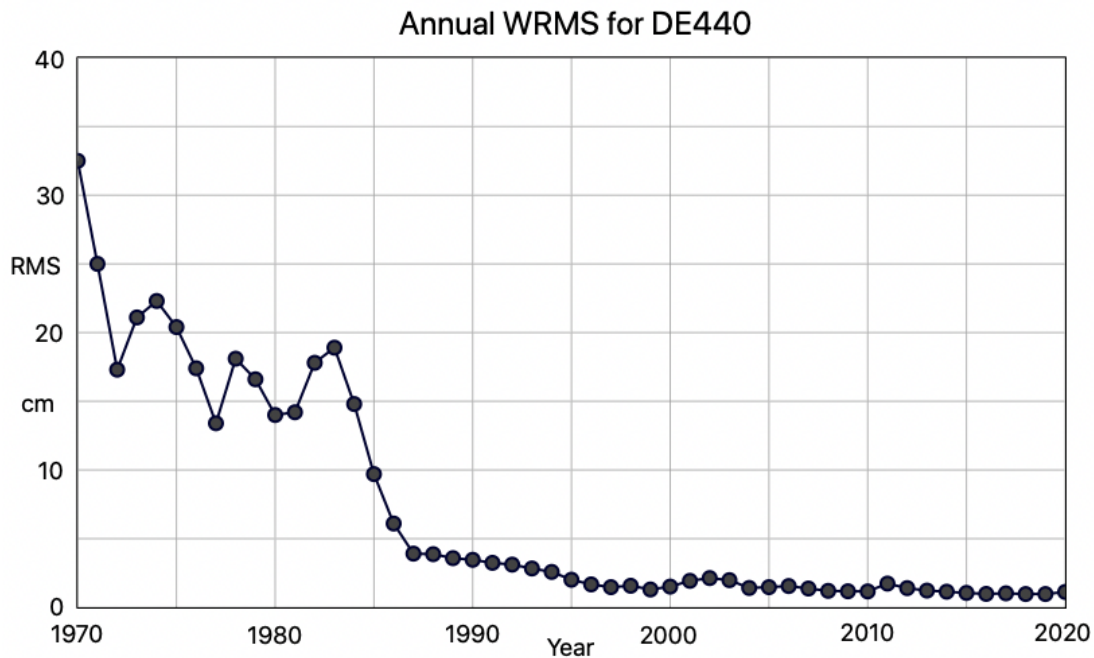
Figure 1. Annual weighted rms residuals for DE440, 1970 – March 2020.

Figure 2. Annual weighted RMS residuals from 1987 – March 2020.

A worldwide network of satellite laser ranging (SLR) stations and LLR stations is coordinated by the International Laser Ranging Service (ILRS) [*Pearlman et al*., 2002], but only a few laser sites can range the distant Moon. To set the scale, the semimajor axis of the lunar orbit is 384,399 km, the mean radius of the Earth is 6371 km, and the mean radius of the Moon is 1737 km. Moving at a speed of 299,792.458 km/sec, a laser pulse takes ~2.5 sec to make the round trip. Reviews of the LLR technique are available from *Dickey et al*. [1994], *Murphy* [2013], and *Müller et al.* [2019].

This memo describes the model used in 2020 by the program LPRED to calculate an LLR time of flight and compare with an observed value to get a residual. It updates a previous memo (*Williams and Boggs*, 2015). This memo is more detailed than an outline, but it is still an overview. Many details are lacking and some familiarity with astronomical and geophysical processes and nomenclature is assumed. We note that the design and construction of an analysis program is a compromise between accuracy and pragmatism.

For the terrestrial model, the IERS Conventions (2010) [*Petit and Luzum*, 2010] is an indispensible companion to this memo. We make frequent reference to sections of that document. The models for spacecraft navigation are another invaluable resource [*Moyer*, 2000]. Here we do not describe the numerical integration programs for calculating solar system orbits and lunar rotation. There are two integration programs at JPL that embody very similar physical models. These dynamical models are described by *Park et al*. [2020]. Since 2014 we have added geodetic precession to the integrated physical libration

model, solar Lense-Thirring effect to the integrated orbits, a t^2 term to the Earth's J_2 that perturbs the lunar orbit, and solar radiation pressure affecting the lunar orbit.

2. LLR Range Data

The transmit time at the ranging station is denoted T1, the time of the reflection is T2, and the receive time is T3. The round-trip light time Δt = T3−T1 is about 2.5 sec, but it varies ±7% from about 2.3 to 2.7 sec. The observed round-trip light time Δt gives the one-way "range" ρ when multiplied by half the speed of light c, $\rho \approx c\Delta t/2$, or 15 cm/nanosec. Since the Moon moves ~2.5 km and the Earth rotates ~1 km while the laser pulse is in flight, the foregoing one-way range is a convenient approximation rather than a geometric range at a single time.

Multiple detections of one or more photons are combined into less frequent normal points. Each normal point may combine several minutes to several tens of minutes of photon returns. An LLR observation includes the transmit date and time in UTC (Coordinated Universal Time), receive minus transmit time in UTC seconds (round-trip light time), station and retroreflector array IDs, number of photons, a range uncertainty, and the laser wavelength. Environmental parameters include atmospheric pressure, temperature, and relative humidity at the station. The normal point may also have its time span, the signal-to-noise ratio, and an indicator for the quality of the range identification.

The annual number of normal points is shown in Fig. 3 for three transmitted laser colors.
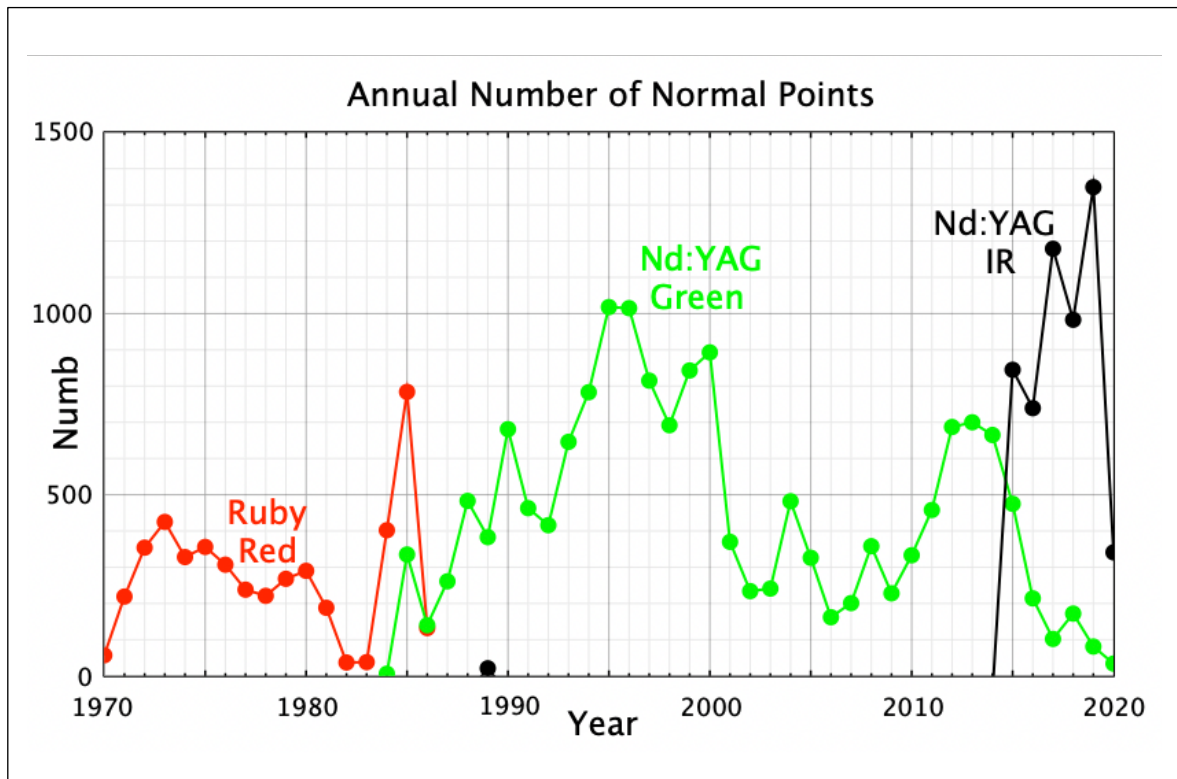
Figure 3. The annual number of normal points in DE440 for 3 transmitted laser colors.

The lunar laser ranging stations at McDonald Observatory, Texas; Observatoire de la Côte d'Azur, France; Haleakala Observatory, Hawaii; Apache Point Observatory in New Mexico; and Matera, Italy provided the extended data sets that are analyzed by the LLR programs. Shorter data sets are available from Crimea in 1974 and the 1980s, then in the Soviet Union, and Wettzell, Germany, 2018 – 2020. The number of ranges and their time spans are given in Table 1. Collections of LLR data are available from the International Laser Ranging Service archives at

　　　ftp://cddis.gsfc.nasa.gov/pub/slr/data/npt_crd/
　　　ftp://edc.dgfi.tum.de/pub/slr/data/npt_crd/

and from the Paris Observatory Lunar Analysis Center at
　　　http://polac.obspm.fr/llrdatae.html .
For Apache Point normal points, consult
　　　http://physics.ucsd.edu/~tmurphy/apollo/norm_pts.html
for ranges and notes.

Table 1. Observations from LLR stations, March 1970 to March 2020.

Station	Number of Ranges	Time Span
McDonald 2.7 m, Texas	3440	1970 – 1985
MLRS, Saddle site, Texas	275	1985 – 1988
MLRS, Mt. Fowlkes site, Texas	2870	1988 – 2013
Crimea, USSR	28	1974, 1982 – 1984
Observatoire de la Côte d'Azur, France	16425	1984 – 2020
Haleakala, Hawaii	694	1984 – 1990
Apache Point, New Mexico	2452	2006 – 2016
Matera, Italy	248	2003 – 2020
Wettzell, Germany	70	2018 – 2020
Total	26502	1970 – 2020

There are five target retroreflector arrays on the Moon. These flat arrays of corner cubes are located at the three Apollo 11, 14, and 15 landing sites and on the Lunokhod 1 and 2 rovers delivered by the Luna 17 and 21 landers. The Apollo 15 array at the Hadley site is the largest and it provides the strongest returned signal. Table 2 provides some statistics.

Table 2. Observations obtained from retroreflector arrays, March 1970 to March 2020.

Lunar Site	Number of Ranges	Percentage	Time Span
Apollo 11, Tranquility	3172	12.0%	1970 – 2020
Apollo 14, Fra Mauro	2993	11.3%	1971 – 2020
Apollo 15, Hadley	17448	65.8%	1971 – 2020
Lunokhod 1	1260	4.8%	1974, 2010 – 2020
Lunokhod 2, Le Monnier	1629	6.1%	1973 – 2020
Total	26502	100%	1970 – 2020

Apollo 11 landed in 1969 and was ranged shortly after, but our data set eliminates the less precise 1969 ranges and starts in March 1970. The location of Lunokhod 1 was not known well enough to range until it was found in 2010 [*Murphy et al.*, 2011]. Recently, observations during 1974 at Crimea were located [*Yagudina et al.*, 2018].

3.1 LLR Model

We need to compare the observed Δt = T3−T1 to a computed value in order to fit the model parameters to observations. The model for the computed value is the subject of this section.

3.2 MJD and JD

The calendar date and transmit time are converted to Modified Julian Day (MJD) and Julian Day (JD), JD = MJD + 2400000.5. For example, noon on January 1, 2000 is MJD 51544.5 and JD 2451545.0. The example is the J2000 reference time. (Note that the D in JD and MJD stands for "day", not the corruption "date.")

3.3 Station Location

To the Earth-fixed geocentric ranging station spherical coordinates at J2000, the LLR software adds slow linear station motion in the radial, east, and north directions for Year(T1)−2000. For T1 in years

$$\mathbf{R}_{\mathrm{STN}}(T1) = \mathbf{R}_{\mathrm{STN}}(2000) + \frac{d\mathbf{R}_{\mathrm{STN}}}{dt}(T1 - 2000) \ . \tag{1}$$

Station motion is typically a few mm/yr vertically and a few cm/yr horizontally. Station coordinates typically refer to the intersection of axes of the mount. For most stations, the transmitting and receiving telescopes coincide, but they were separate at the Haleakala site.

3.4 Air **Pressure Loading and Center of Mass Motion**

A local increase in air pressure depresses the Earth's surface. This is a small correction of no more than a few millimeters. The LLR software approximates loading from atmospheric pressure variation with a perturbation of the vertical coordinate of

$$\Delta R = \partial R/\partial P \ \Delta P, \tag{2}$$

where ΔP is the pressure variation about the mean. See Table 3 for the rms pressure and radial variations by station. Although this radial variation and some of the partials $\partial R/\partial P$ are approximations, the effect is only a few millimeters. The IERS Conventions (2010) discusses effects on station position in chapter 7. The effect of diurnal and semidiurnal pressure variations are in section 7.1.3. At the LLR sites, they are <1 mm and we do not include them in the model.

Table 3. Mean pressure and RMS pressure variation, and the influence on the vertical coordinate.

Station Site	Mean Pressure, mbar	RMS Pressure Variation, mbar	$\partial R/\partial P$ mm/mbar	RMS Radial Variation, mm
McDonald 2.7 m, Texas	798	4	−0.47	1.8
MLRS Saddle, Texas	808	3	−0.47	1.4
MLRS Mt. Fowlkes, Texas	800	4	−0.47	1.7
OCA/MEO, France	875	7	−0.34	2.2
Haleakala, Hawaii	709	2	−0.15	0.3
Apache Point, New Mexico	728	4	−0.48	1.7
Matera, Italy	962	4	−0.27	1.1
Wettzell, Germany	944	4	−0.44	1.7
Crimea, Soviet Union	949	3	−0.25	0.9

Seasonal mass variations of atmosphere and oceans cause an annual translation of the center of figure of the Earth with respect to the center of mass (*Wu et al.*, 2012, 2017). We apply the following correction to the center of figure coordinates of stations to get center of mass coordinates

$$\Delta R_j = -A_j \cos\left(\frac{2\pi}{365.25}\left(t - J2000 - \delta t_j\right)\right) , \qquad (3)$$

where ΔR_j are the corrections to the three coordantes, A_j are the three coefficients, δt_j corrects day of year to zero phase, and t is MJD. We use the amplitudes and phase-related times in *Wu et al.* (2017). The corrections are small, a few millimeters in size.

3.5 UT1 and Polar Motion at T1
An input table of TAI−UT1, and polar motion X and Y is interpolated at the MJD value. UT1 follows the variable daily rotation and polar motion describes the axis of daily rotation (not the instantaneous spin axis) with respect to the body axes. The Earth's equator rotates with a speed of 465 m/sec, so UT1 values accurate to ~2 μsec are needed for 1 mm global rotation accuracy.

3.6 Solid-Body Pole Tide

As the Earth's axis of rotation moves with respect to its body, the oblate shape tends to follow the moving axis. The pole tide is computed for $X-X_P$ and $Y-Y_P$, where $X_P=0.056''+0.0021''$/yr (Year–2000) and $Y_P=0.346''+0.0037''$/yr (Year–2000) in the LLR software. The IERS Conventions advocates third degree polynomials for X_P and Y_P. The resulting pole tide distortion is added on to the station vector. The subtraction of X_P and Y_P is intended to separate out the annual wobble and (14 month) Chandler wobble so that appropriate Love numbers ($h_2=0.6207$ and $l_2=0.0836$) can be used for that frequency band. For the coefficients of IERS Conventions equation (7.26), the LLR software uses 32.4 mm/$''$ for the radial component and 9 mm/$''$ for the horizontal components. The 32.4 mm/$''$ coefficient is 2% smaller than the value in the Conventions, but loading at the LLR stations from the ocean's pole tide will reduce the coefficient by a few percent. The combined annual and Chandler wobbles can reach ~0.3$''$ maximum, so the radial variation can reach ±1.0 cm and the horizontal variation can reach ±3 mm. What happens to the distortion due to the linear or slow polynomial parts of X and Y? It depends on larger Love numbers and it becomes part of station motion. The radial rate from the linear motion could reach 0.4 mm/yr.

3.7 Time Transformations at T1

Although the LLR observations are measured with UTC, the JPL lunar and planetary ephemeris uses Barycentric Dynamical Time (TDB), a time appropriate for coordinates referred to the center of mass (barycenter) of the solar system. The UTC transmit time is first transformed to International Atomic Time (TAI). The latter is a continuous time scale, whereas UTC has discontinuities designed to keep UTC close to UT1, a "time" based on the rotation of the Earth. Over the decades spanned by the LLR data, those discontinuities accumulate; from mid-2012 until mid-2015 TAI=UTC+35 sec. From mid-2015 to the start of 2017, TAI−UTC is 36 sec, and subsequently up to 2020 the difference is 37 sec. Adding 32.184 s to TAI would give Terrestrial Time (TT), TT=TAI+32.184 sec. Prior to 1972 there were also discontinuous UTC rate changes that require corrections to the length of the second used for ranges before 1972.

The transformation from TT or TAI to TDB involves relativistic effects. Viewed from the solar system barycenter, terrestrial clock rates vary as the velocity and external potential at the center of the Earth change as the Earth follows its path about the Sun. We present the transformation in two parts: one depends on the position of the station with respect to the Earth's center, and the other depends only on the orbital motion of the Earth. The station, which is displaced from the center of the Earth, experiences a rotational velocity and a slightly different solar potential than the geocenter. With both effects, the clock rates are connected by

$$\frac{dTDB}{dTAI} \approx 1 - L_B + \frac{(\mathbf{v_E} + \mathbf{v_S})^2}{2c^2} + \frac{(U + \mathbf{R_S} \bullet \nabla U)}{c^2} \ , \tag{4}$$

where U is the (positive) external potential from the Sun, Moon, and planets at the geocenter, $\mathbf{v_E}$ is the velocity of the Earth's center with respect to the solar system barycenter, $\mathbf{v_S}$ is the velocity of the station with respect to the Earth's center, and $\mathbf{R_S}$ is

the vector from the geocenter to the station. The $\mathbf{R_S} \bullet \nabla U$ term is an expansion of the potential for the station displaced by $\mathbf{R_S}$ from the geocenter. The $L_B = 1.550519768 \times 10^{-8}$ removes the mean rate from the velocity and potential terms.

The $\mathbf{v_E} \bullet \mathbf{v_S}/c^2$ part of eq. (2) can be integrated by parts to get a daily $\mathbf{v_E} \bullet \mathbf{R_S}/c^2$ variation in time. The daily correction can reach ± 2.1 µsec. The second term from the integration by parts is small enough to ignore.

$$TDB \approx TAI + \frac{\mathbf{v_E} \bullet \mathbf{R_S}}{c^2} + 32.184 \text{ sec} + \text{Orbit Terms} \tag{5}$$

For the idealized case of a massless Earth in an elliptical orbit

$$TDB \approx TAI + \frac{\mathbf{v_E} \bullet \mathbf{R_S}}{c^2} + \frac{2\mathbf{r_E} \bullet \mathbf{v_E}}{c^2} + 32.184 \text{ sec} \ , \tag{6}$$

where $\mathbf{r_E}$ is the position of the Earth's center with respect to the solar system barycenter. For perturbed orbits, the $2\mathbf{r_E} \bullet \mathbf{v_E}/c^2$ term can be replaced with an integrated value, a series, or a function of ephemeris positions and velocities. The Earth's ephemeris is interpolated from the ephemeris file to get $\mathbf{r_E}$, $\mathbf{v_E}$, and potential. For the TAI to TDB transformation, the largest of the periodic terms, the "elliptical" term, is a 1.66 msec annual term that passes through zero phase in early January, but there are smaller effects from Jupiter (22 µsec), Saturn (5 µsec), and the Moon (2 µsec) [*Moyer*, 1981ab; *Fairhead and Bretagnon*, 1990; *Harada and Fukushima*, 2003]. Note that in the 2.5 s of the round-trip light time, the daily term can change up to 0.4 ns and the annual term can change by 0.8 ns. These relativistic corrections alter the computed Δt interval and are necessary for accurate LLR analyses. The LLR software uses Moyer's formulation that depends on ephemeris positions and velocities of the Earth, Moon, Sun, and planets. Though only accurate to a few µsec, that accuracy is sufficient for range computation accuracies <1 mm. There are two requirements, one on the radial position accuracy at a time and the other on the change in TDB−TAI during the ~2.5 s round trip. Since the Moon's radial velocity is <100 m/sec the first only requires 10 µs accuracy. The second requirement requires 12 µs accuracy for the amplitude of the annual term, 6 µs at 1/2 yr, and 1 µs accuracy at 1 month. *Moyer* [1981b], *Fairhead and Bretagnon*, [1990], and *Harada and Fukushima*, [2003] present trigonometric series. The latter two are extensive and very accurate series. As an alternative, eq. (4) can be integrated numerically. A very accurate numerically integrated version of TDB−TT is available with the DE440 ephemeris [*Park et al.*, 2020].

The relativistic time corrections are iterated. Expressions (5) and (6) require the orientation of the station vector with respect to the Earth's velocity in a consistent frame, the station vector is rotated from a body-fixed frame to a space-fixed frame allowing for UT1, polar motion, precession, and nutation. Tides are too small to make a significant difference for relativity. Expression (5) is calculated with the Moyer series for the orbital terms. With iteration, the UTC value at T1 is converted to TDB.

The LLR software does not introduce the average rate differences that are part of the Geocentric Coordinate Time (TCG) and Barycentric Coordinate Time (TCB) scales (chapter 10 of the IERS Conventions). The fractional changes in these two rates are denoted L_G and L_C, respectively, which combined give L_B. As a consequence, there are differences in the length scales that will be addressed below (§ 3.10). We also note that, with the notation in chapter 10 of the IERS Conventions, $TDB_0 \approx -P_0 \approx -P(T_0) \approx -65.5$ μsec. The LLR software does not introduce this constant, which appears in the TT to TCB transformation, into the TAI to TDB transformation. The TDB_0 constant should be used with a numerically integrated TDB−TT value because it is the value of the series at the lower limit of the integration. It should not be used with the series.

3.8 Earth Orientation at T1

The station's orientation in space depends on terrestrial UT1, polar motion, precession, and nutation. The precession of the equinox and the evolution of the obliquity $\varepsilon_A(t)$ are computed with polynomial expressions. The IAU 2006 expressions for precession angles ζ_A, θ_A, and z_A and obliquity ε_A are given by *Hilton et al.* [2006]. The "time" tracking the angle of rotation of the Earth with respect to the precessing equinox, the Greenwich Mean Sidereal Time (GMST), is a polynomial function of UT1. An expression for GMST in seconds that is compatible with the IAU 2006 precession polynomials comes from evaluating eq. (33) in *Williams* [1994].

$$GMST = 24110.54841 + 8640184.7944792 \, T_U + 0.0927722 \, T_U{}^2 - 2.0 \text{x} 10^{-6} \, T_U{}^4$$
$$+ \text{Mod}(UT1, 86400) \tag{7}$$

In centuries $T_U = [(\text{MJD}-51544.5)+(\text{UT1}-\text{MJD})]/36525$, where UT1−MJD is expressed in days. The large coefficient of T_U causes the number of terrestrial rotations per year to be one more than the number of solar days in a year. The nonlinear terms do not imply nonuniform rotation with respect to space for uniformly increasing UT1. Rather they reflect the nonlinear motion of the mean equinox. The cubic term is sufficiently close to zero to ignore. The UT1 in the Mod function includes fast variations.

The nutation angles are $\Delta\psi$ for (left-handed) ecliptic longitude and $\Delta\varepsilon$ for obliquity., The equation of equinoxes $\Delta\psi\cos\varepsilon_A(t)$ can be added on to GMST. With additional terms at the period (18.6 yr) and half period (9.3 yr) of the lunar node, we get Greenwich Sidereal Time (GST). With GMST and $\Delta\psi$ in seconds of arc, then

$$GST = GMST + \Delta\psi\cos\varepsilon_A(t) + 0.00264 \sin\Omega + 0.000063 \sin 2\Omega \tag{8}$$

The node-related corrections are a dynamical consequence of the motion of the equinox and obliquity.

UT1 and polar motion X and Y include small semidiurnal and diurnal tidal variations. The small rapid UT1 and polar motion corrections are added on to the interpolated values from the input table (§ 3.5). In the LLR software the fast variations arise from the M2, S2, K2, N2, K1, O1, P1, Q1, and sidebands of the K1 and O1 tides. Table 4 lists the 10 corresponding arguments. The combined Tables 8.3a, 8.3b, and 5.1b of the IERS

Conventions give the amplitudes for UT1 and combined 8.2a, 8.2b, and 5.1a give amplitudes for polar motion. The largest examples of these corrections, ~1 cm, occur for the M2, K1, and O1 tides.

Table 4. Four semidiurnal and six diurnal tidal arguments. For the angles in the arguments: G is GMST, l is lunar mean anomaly, F is lunar mean argument of latitude, Ω is lunar node, D is mean elongation of the Moon from the Sun, mean lunar longitude is $L=F+\Omega$, and mean solar longitude is $L'=L-D$.

Name	Argument	Period in days
K2	$2G$	0.498635
S2	$2G-2L'$	0.500000
M2	$2G-2L$	0.517525
N2	$2G-2L-l$	0.527431
K1 sideband	$G-\Omega$	0.997123
K1	G	0.997270
P1	$G-2L'$	1.002745
O1	$G-2L$	1.075806
O1 sideband	$G-L-F$	1.075976
Q1	$G-2L-l$	1.119515

To rotate the station vector from an Earth-fixed frame to a J2000 space-related frame, the sequence of rotations is

$$\mathbf{R_3}(\zeta_A-90^\circ)\,\mathbf{R_1}(-\theta_A)\,\mathbf{R_3}(90^\circ+z_A)\,\mathbf{R_1}(-\delta_X)\,\mathbf{R_2}(-\delta_Y)\,\mathbf{R_1}(-\varepsilon_A)\,\mathbf{R_3}(\Delta\psi)\,\mathbf{R_1}(\varepsilon_A+\Delta\varepsilon)\,\mathbf{R_3}(-\text{GST})\,\mathbf{P}(X,Y)\,,$$
$$(9)$$

where $\mathbf{P}$ is a matrix for polar motion X and Y, δ_X and δ_Y are small rotations of the Earth's orientation, and $\mathbf{R_1}$, $\mathbf{R_2}$, and $\mathbf{R_3}$ are rotation matrices about the first, second, and third axes. The LLR software can solve or correct for small rotations δ_X and δ_Y at the time of observation that include (equinox and obliquity related) constant rotations, (precession and obliquity related) rates, and corrections to periodic nutation terms at 18.6 yr, 9.3 yr, 1 yr, 1/2 yr, and 1/2 month. A positive rotation of a vector is equivalent to a negative rotation of the frame.

Terrestrial orientation accurate to 0.03 mas is needed for 1 mm station vector accuracies in space. The LLR software does not implement all of chapter 5 of the IERS Conventions. Also, it does not apply a nominal value for the variable free core nutation (FCN) at 430.2 days (retrograde), which is <0.3 mas in size.

3.9 Solid-Body Tides on Earth

The main tidal displacement of the station is caused by degree-2 tides raised by the Moon and Sun. Vertical lunar tides can vary between +27 and −14 cm and solar tides span +10 to −5 cm. Horizontal tides can reach ±5 and ±2 cm. For degree-2 elastic tides with vector $\mathbf{u}$ pointing from the center of the Earth toward the surface station and $\mathbf{u}'$ pointing toward the tide-raising body, the station displacement is

$$\Delta \mathbf{R} = \frac{M'R^4}{mr'^3} \left\{ \frac{h_2}{2} \left[3(\mathbf{u} \bullet \mathbf{u'})^2 - 1 \right] \mathbf{u} + 3l_2 (\mathbf{u} \bullet \mathbf{u'}) \left[\mathbf{u'} - (\mathbf{u} \bullet \mathbf{u'}) \mathbf{u} \right] \right\} \quad . \tag{10}$$

The radius of the Earth is R, its mass is m, the mass of the tide-raising body is M', and its distance is r'. Degree-3 tides are also computed. They are much smaller than the degree-2 tides. Our nominal degree-2 Love numbers are h_2=0.6078 and l_2=0.0847 and the degree-3 values are h_3=0.292 and l_3=0.015. These values are compatible with the real values recommended in chapter 7 of the IERS Conventions. Moon-raised third-degree tides on the Earth are only 1.7 mm high and Sun-raised third-degree tides are very small. The evaluation of equation (10) includes a constant part, which is not modified.

There are corrections to the global degree-2 tidal calculations. They arise from two causes: the oblate core-mantle boundary, and tidal dissipation. Both causes affect in-phase tides; dissipation also shifts the phase. The software applies in-phase and out-of-phase corrections to the vertical tides for the 10 tidal components of Table 4. The largest correction is 12 mm for K1. The K1 sideband shifts 2 mm and the P1 tide shifts 1 mm. Extensive tables are given in chapter 7 of the Conventions. The horizontal correction is <1 mm and is ignored.

For each station, 3-dimensional (up, east, north) ocean loading tides are computed for the 10 tidal arguments in Table 4. The coherent center of mass correction is included. The stations in Table 1 have extensive observations and we input tables that are based on the FES2004 tidal model. For the continental LLR sites, ocean loading amplitudes are less than 1 cm, but for the mid-ocean Haleakala site 3 amplitudes exceed 1 cm. The ocean loading website at http://holt.oso.chalmers.se/loading/ is established by M. S. Bos and H.-G. Scherneck.

The LLR software departs from the IERS Conventions in several ways. The evaluation of the main tidal distortion from equation (10) uses real Love numbers; the phase-shifted components are evaluated separately. For the small global and ocean loading corrections, the software does not attempt to correct the slow zonal tides, since those corrections are predicted to be <1 mm. Also, we question whether the corrections can be extrapolated to 18.6 yr using an Andrade-type function; that type of extrapolation does not work for long period tides on the Moon [*Williams and Boggs*, 2015]. The LLR software does not implement the latitude dependence of the Love numbers, a 0.1% correction (<1 mm) for vertical tides. The IERS Conventions document uses different phase conventions than the ocean loading website. Also, the two ocean loading formats appear to use different directions for horizontal tides. Analysts need to be careful with details. The LLR software uses cosines and sines of the arguments in Table 3. We have our own solid-body tidal expansion, which we used to confirm the global corrections and their phases. The FES2004 ocean model with output in the HARPOS format was the source for the LLR ocean loading tables, but we altered the phases to match the arguments in Table 4.

3.10 Relativistic Adjustments to the Station Vector

We need to transform the geocentric station vector $\mathbf{R_S}$ from a terrestrial frame compatible with TAI or TT to the solar system barycentric frame compatible with TDB. The Lorentz contraction of $\mathbf{R_S}$ is

$$-\frac{\mathbf{v_E} \bullet \mathbf{R_S}}{2c^2}\mathbf{v_E} \quad . \tag{11}$$

The Earth's speed is ~30 km/sec so the Lorentz contraction of the Earth is ~3.2 cm in the velocity and anti-velocity directions.

In addition, there is a relativistic adjustment to the scale of $\mathbf{R_S}$

$$\left(1 - L_C - \frac{U_E}{c^2}\right)\mathbf{R_S} \quad , \tag{12}$$

where the scale parameter is $L_C = 1.480827 \times 10^{-8}$ and U_E is the geocentric solar potential GM_S/r_{SE} that depends on solar mass M_S and distance r_{SE}. The scale change is 16 cm and there is a ±1 mm annual variation due to the eccentricity of the solar orbit. The effect on scale from the potential due to the Moon and planets is very small and is ignored. IERS Conventions section 11.2 deals with these spatial adjustments.

3.11 Up-Leg Light Time Iteration for T2, Position, and Orientation of the Moon

The T1 time is established in UTC and TDB, so the next step is to compute T2, the time of reflection. Because the Moon is moving ~1 km/sec with respect to the Earth and the Earth is rotating 465 m/sec at the equator, the T2 computation requires iteration. As a first approximation to T2, to start the iteration half of the observed light time is added on to T1. The position of the Moon with respect to the Earth and solar system barycenter is obtained from a numerically integrated ephemeris (e. g., DE440 [*Park et al*., 2020]]). At the T2 time, the orientation of the Moon (physical libration Euler angles) is obtained from the ephemeris file, the rotation matrix between the lunar body and space frames is set up, and the Moon centered retroreflector vector is rotated into the space-fixed frame.

Unlike the Earth, it is not necessary to transform the T2 time to a Moon centered or surface related frame. The latter would be necessary if one-way ranges relied on a clock on the lunar surface.

3.12 Tidal Displacement on the Moon

Earth caused vertical degree-2 tides on the Moon vary by roughly ±0.1 m, see Figure 4. Horizontal tides vary by about half of that amount, see Figure 5. Equation (10) is evaluated with the radius of the Moon for R and the lunar mass for m. Time-varying tides caused by the Sun are ~2 mm in height. Degree-3 tides are <1 mm, but are calculated. Appropriate model Love numbers are $h_2=0.0423$ and $l_2=0.0107$, $h_3=0.0234$, and $l_3=0.0030$ [*Willliams et al*., 2014b; *Williams and Boggs*, 2015]. The degree-2 Love numbers can be either input or solution parameters.
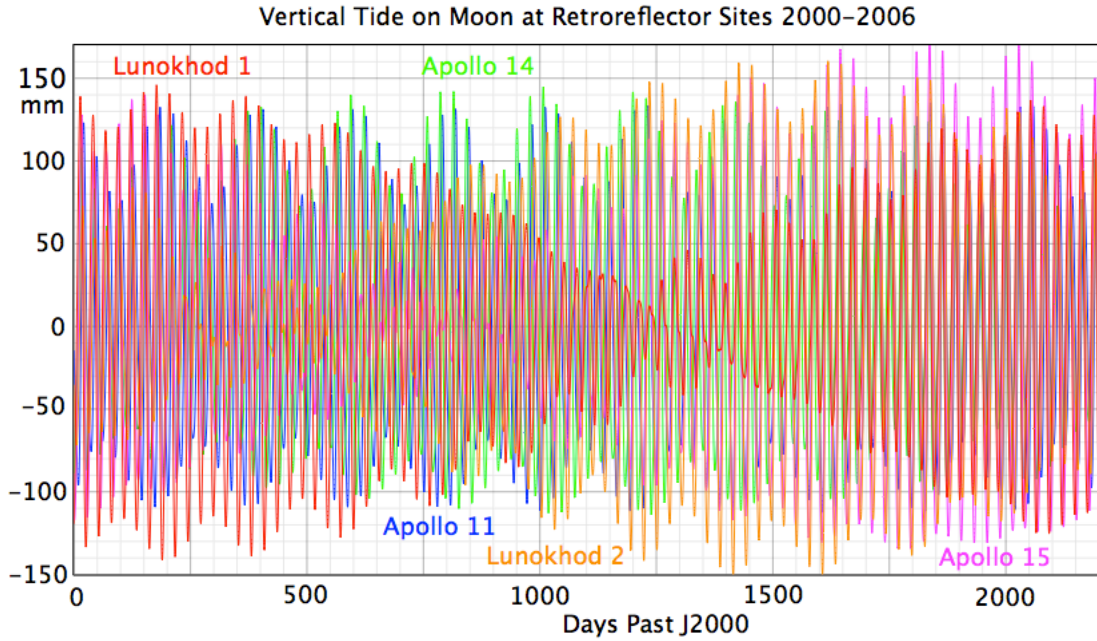
Figure 4. Vertical elastic tides at the five retroreflector locations for interval 2000–2006.
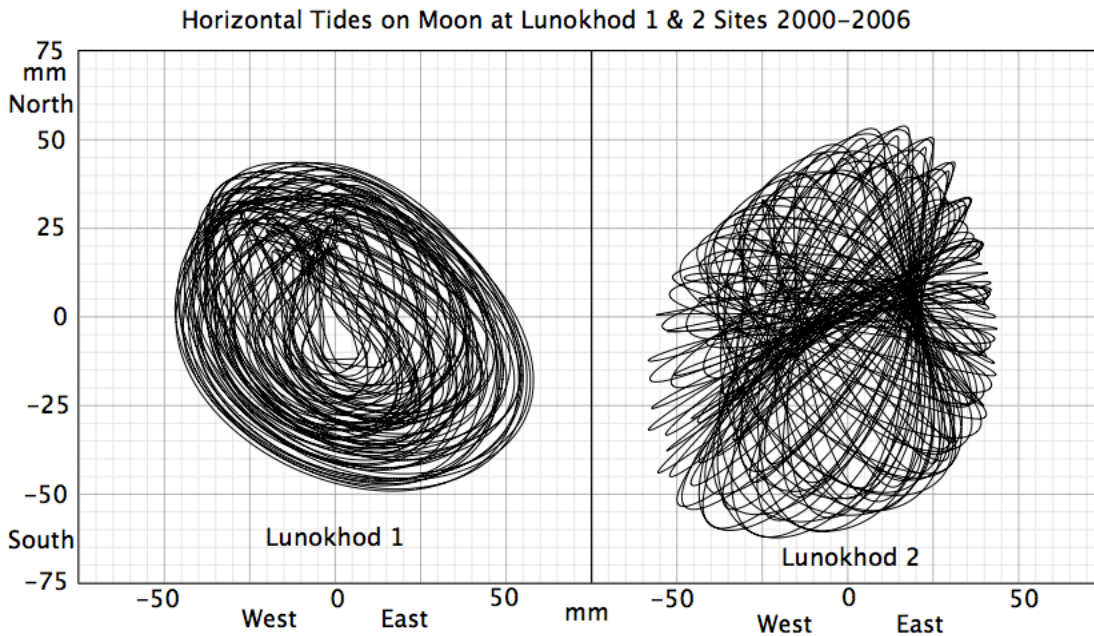
Figure 5. Horizontal tides at the Lunokhod sites for the interval 2000–2006.

The effect of tidal dissipation is added for the two largest tides with periods of 27.555 d for argument l and 27.212 d for F. Small cosine and sine corrections are added from an internal table for the 5 retroreflector sites (Appendix A1). The dissipation factors h_2/Q_h for vertical and l_2/Q_l for horizontal may be either input or solution parameters. The size of the dissipation correction is ~2 mm or less.

Appendix A2 has the constant tidal components (X, Y, Z, Up, East, North) for the 5 retroreflector sites. The elastic values are given for the DE440 displacement Love numbers. The table results from phase shifting the lunar tidal variations in *Williams and Boggs* [2015].

There is a pole tide on the Moon due to changes in the direction of the spin vector; see Appendix C of *Williams and Boggs* [2015] for the potential and rotation rate terms. The size is calculated to be <0.2 mm. Consequently, it is not included in the model for lunar displacement.

3.13 Thermal Expansion of Reflectors

The retroreflectors are subject to large monthly variations of temperature. At the equator, the lunar surface can reach ~386º K during the day (albedo 0.08) and ~100º K at night. Although the corner cubes have low thermal expansion coefficients, the Lunokhod rovers and the aluminum structures of Apollo reflectors expand and contract by one (Apollos) to several (Lunokhods) millimeters during the 29.5 d synodic month. Accurate thermal models are complicated. This section presents simplified models that depend on heating by the Sun and heating from the lunar surface.

The simplest model has the retroreflector temperatures T proportional to the lunar surface temperature. Using a constant temperature at night, the day–night temperature difference is proportional to

$$G(T) = \begin{cases} 1.36 \left(\frac{\cos z}{\cos \phi}\right)^{\frac{1}{4}} - 0.36 & \text{if } \cos z > 0.0049 \cos \phi \\ 0 & \text{if } \cos z \leq 0.0049 \cos \phi \end{cases} \tag{13}$$

where z is the zenith angle of the Sun and ϕ is the latitude of the lunar site. The vertical displacement is proportional to $X_T\, G(T)$, where X_T is the vertical variation. The Lunokhod arrays are offset forward and to the right of the rover center so there is also a horizontal displacement proportional to $G(T)$.

Equation (13) would be good if the Apollo retroreflectors were horizontal. A more complicated model allows for the tilt of the Apollo retroreflectors. For the Apollo arrays oriented perpendicular to the mean Earth direction, there is primary heating by the Sun and secondary heating from the lunar surface.

$$G(T) = \begin{cases} 1.15(\cos \eta + 2.30 f \cos z)^{\frac{1}{4}} - 0.38 f^{\frac{1}{4}} \cos^{\frac{1}{4}} \phi & \text{if } \cos \eta > 0, \cos z > 0 \\ 1.42 f^{\frac{1}{4}} \cos^{\frac{1}{4}} z - 0.38 f^{\frac{1}{4}} \cos^{\frac{1}{4}} \phi & \text{if } \cos \eta \leq 0, \cos z > 0.0049 \cos \phi \\ 0 & \text{if } \cos z \leq 0 \end{cases}$$
$$\tag{14}$$

Angle η is between the solar direction and the normal to the array face. The Apollo arrays are insulated on bottom and sides; f gives the fraction of the lunar surface seen by

14

the top face of the reflector. For the numerical factor X_T of $G(T)$ to be the maximum vertical displacement, the numerical coefficients are similar for the 3 Apollo reflectors, and eq. (14) is compatible with the 3 maximum displacements to ~4%. The fraction f that depends on the nominal array tilt is given in Table 5.

Allowing for the nearly vertical sides of the Lunokhod rovers, there is heating from the lunar surface and from direct sunlight.

$$G(T) = \begin{cases} 1.31 \left[\frac{(\cos z + 0.1 \sin z)}{\cos \phi} \right]^{1/4} - 0.33 & \text{if } \cos z > 0 \\ 0 & \text{if } \cos z \leq 0 \end{cases} \tag{15}$$

We had to guess the thermal properties of the Lunokhod rovers so the 0.1 factor of $\sin z$ for the sides is approximate. Multiply $G(T)$ by the maximum vertical displacement X_T. Note that the two Lunokhod rovers are similar, but not identical. Lunokhod 1 has the lid closed whereas Lunokhod 2 has the lid open. Also, the tub dimensions are somewhat different. For the ratio of horizontal to vertical displacements see Table 5. For example, a 5 mm vertical expansion would be accompanied by a 6 mm expansion forward and a 2 mm expansion to the right side. The rovers are supposed to be oriented toward the azimuth of the mean Earth direction.

Table 5. Ratio of offsets of arrays from the spacecraft center at ground to height and also fraction f seen of lunar surface and tilt to mean Earth direction.

Reflector	Forward	Left	Up	f	Tilt	
Ap 11	0	0	1.0	0.13	23.5°	
Ap 14	0	0	1.0	0.10	17.9°	
Ap 15	0	0	1.0	0.14	26.4°	
Lk 1	1.25	-0.4	1.0	1.0	50.0°	
Lk 2	1.25	-0.4	1.0	1.0	39.5°	

Figure 6 shows the temperature function $G(T)$ for several reflectors. The black line is eq. (13) that mimics the lunar surface temperature. Equation (14) is evaluated for Apollos 11 and 14. Sunrise at Apollo 11 and sunset at Apollo 14 illuminate the rear of the reflectors, which are insulated. Heating for that part of the curves comes from the lunar surface. Apollo 15 will be close to the black line. The two Lunokhods have similar curves from eq. (15) represented with red.

The Apollo reflectors are low, a few decimeters, and are expected to vary by 1–1.5 mm. The Lunokhod arrays are 1 m high and might vary by 5 mm vertically. The software can solve for the vertical expansion coefficients X_T for the 5 reflectors. We tried the simple thermal expansion model of eq. (13) and the two component models of eqs. (14) and (15). The improvement in the rms residual was slight for both approaches. Thermal expansion correlates with the equivalence principle test.
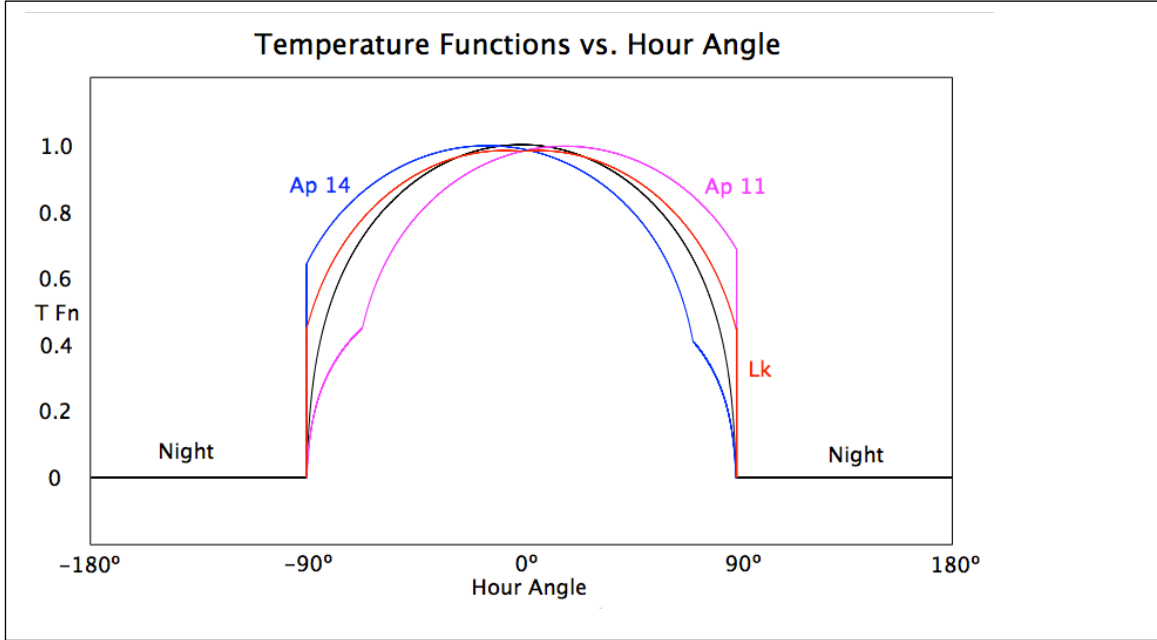
Figure 6. Temperature functions $G(T)$. The black curve mimics the lunar surface temperature. The colored curves are for individual retroreflectors.

3.14 Lorentz Contraction and Relativistic Scale at the Moon

We need to transform the Moon centered reflector vector $\mathbf{R_R}$ from a lunar frame to the solar system barycentric (SSB) frame compatible with TDB. Analogous to section 3.10, the Lorentz contraction is

$$-\frac{\mathbf{v_M} \bullet \mathbf{R_R}}{2c^2}\mathbf{v_M} \quad . \tag{16}$$

The Lorentz contraction of the Moon's radius is ~9 mm in the velocity ($\mathbf{v_M}$) and anti-velocity directions.

Analogous to the Earth, the Moon centered reflector vector is scaled by

$$\left(1 - L_M - \frac{U_M}{c^2}\right)\mathbf{R_R} \quad , \tag{17}$$

where the scale parameter is $L_M = 1.4825 \times 10^{-8}$ and U_M is the solar potential at the Moon GM_S/r_{SM}. The scale change is about 4 cm and the annual variation is only ±0.3 mm. Though small, the annual variation for Earth and Moon radii combine to cause ±1.3 mm of range signal. The effect on scale from the potential due to the Earth and other planets is small and is ignored.

16

3.15 Up-Leg Range Vector

The vector between the terrestrial station at T1 and the lunar retroreflector at T2 is

$$\boldsymbol{\rho}_{12} = \mathbf{r}_M(T2) + \mathbf{R}_R(T2) - \mathbf{r}_E(T1) - \mathbf{R}_S(T1) \; , \qquad\qquad (18)$$

where $\mathbf{r}_{12} = \mathbf{r}_M(T2) - \mathbf{r}_E(T1)$ is the difference in the solar system barycentric coordinates of the centers of the Earth and Moon. The station vector $\mathbf{R}_S$ and reflector vector $\mathbf{R}_R$ include tidal and relativistic corrections.

3.16 Atmospheric Delay

To get the sine of the elevation angle, the unit vector $\boldsymbol{\rho}_{12}/\rho_{12}$ is dotted with the ranging station's zenith unit vector normal to the Earth's flattened ellipsoid. The atmospheric delay model follows chapter 9 of the IERS Conventions, except that a constant a_3 value is used. The LLR elevation angles are normally above 20º, whereas a_3 mainly affects lower elevations. Ranges from the McDonald 2.7 m (1970–1985) and early OCA (1984–1986) sites used red ruby lasers (0.694 µm), but subsequent ranges use green beams (0.532 µm) from frequency-doubled Nd:YAG lasers. Starting in March 2015, many infrared ranges (1.064 µm) have been obtained at OCA. The model in the IERS Conventions includes a dependence on color. At the zenith and on the geoid, one atmosphere of air delays the range by 2.4 m, so the delay can be ~7 m at 20º elevation. These delays are scaled by the atmospheric pressure at the station with corrections for temperature and humidity.

Table 6. Mean pressure and temperature and their rms scatter for the LLR sites with extensive data sets. Pressures and temperatures were measured during ranging sessions.

Station Site	Mean Pressure, mbar	RMS Pressure Variation, mbar	Mean Temperature, ºC	RMS Temperature Variation, ºC
McDonald 2.7 m, Texas	798	4	14	6
MLRS Saddle, Texas	808	3	11	7
MLRS Mt. Fowlkes, Texas	800	4	14	6
OCA/MEO, France	875	7	9	6
Haleakala, Hawaii	709	2	6	3
Apache Point, New Mexico	728	4	8	6
Matera, Italy	962	4	13	7
Wettzell, Germany	944	4	12	8

Table 6 gives the average pressures at LLR ranging stations with long spans of data. Since the LLR observatories are usually located on mountains, their mean air pressure values are less than sea level, which reduces the atmospheric delay. Nonetheless, an accurate atmospheric delay model is critical. Clear weather correlates with higher pressure biasing the mean pressure.

The earliest span of McDonald data appears to have pressures that are biased low. Prior to February 13, 1971 (MJD 40995) we add 7 mbar to the McDonald pressures. Another oddity, the mean pressure difference between the McDonald 2.7 m site and the Mt. Fowlkes site does not match the height difference.

3.17 Shapiro Delay

Light has a longer path when passing through a gravity field. From a Newtonian perspective, light appears to be slowed. The Shapiro delay [*Shapiro*, 1964] is computed with a logarithmic form.

$$\delta t_j = \frac{(1+\gamma_{PPN})GM_j}{c^3} \ln\left(\frac{r_{Sj}+r_{Rj}+\rho_{12}}{r_{Sj}+r_{Rj}-\rho_{12}}\right) \qquad (19)$$

The gravitating body j has mass M_j at distances r_{Sj} and r_{Rj} from the Earth station and Moon retroreflector, respectively. Scalar ρ_{12} comes from equation (18). The Shapiro time delay is proportional to $(1+\gamma_{PPN})$, and the Parameterized Post-Newtonian γ_{PPN} that characterizes the curvature of space is 1 for general relativity. The average solar potential at a 1 au distance is $<U>/c^2 = 0.99\times10^{-8}$. The Sun caused mean delay for LLR is ~50 nsec, equivalent to ~7.5 m. The annual variation is ±12 cm. The delay due to the Earth's gravity is ~4 cm, but it varies with elevation angle. The delay from the Moon is <1 mm. The delay from Jupiter is ~1.4 mm, but its variation is <1 mm. The LLR software computes the delay from the gravity fields of Sun and Earth, but not the Moon, Jupiter, and other distant planets.

Most of the solar time delay acts like a scale change in the distance, which is not unique, but the ±12 cm annual variation confers some sensitivity to the Parameterized Post-Newtonian γ_{PPN}.

3.18 Corner Cube Delay

The five lunar retroreflectors consist of arrays of solid corner cube prisms. The Apollo corner cubes have a front face diameter of 3.8 cm. The Lunokhod prisms are larger with a triangular front face. There are three reflections in the corner cubes, but it is sufficient to consider the path length from the front face to the vertex. The path length in the fused silica prisms depends on the distance h from the front face to the rear vertex. Delayed by an index of refraction n, the apparent distance from front to bounce is nh so that the T2 bounce point acts like it is $(n-1)h$ behind the vertex. We correct the bounce point to the front face by adding

$$\delta t_{CC} = nh/c \qquad (20)$$

to the computed incoming T2−T1 and outgoing T3−T2 light times. Our derived retroreflector coordinates are at the center of the array at the front face.

The Apollo corner cubes have h=27.5 mm and the Lunokhod prisms have h=43.5 mm. With an index of refraction of 1.4555 (Heraeus) the $(n–1)h$ values are 12.5 mm and 19.8 mm, respectively, and nh values are 40.0 and 63.3 mm, respectively. The one-way delays are then 133 ps and 211 ps. The delays are slightly longer for off-axis rays and the refractive index depends on wavelength, but for our conditions these effects amount to less than 1 mm.

3.19 Biases
We sometimes see a range bias for a station for a certain interval of time. Sometimes the cause can be identified. In the case of Haleakala, there were different combinations of four rings of lenses used for ranging and calibration. Initially, each ring had a separate time delay, but later they were matched up. We have separate biases for those different combinations of rings. In 2015, OCA began to obtain frequent ranges using infrared, while also obtaining ranges in the green. Consequently, we added bias parameters for differences between green and infrared ranges.

The LLR software can apply or solve for biases. A bias δt_b is added on to the computed value of time delay. We also have biases covering the total data span for each station. The path length inside the telescope to the intersection of axes can be difficult to measure accurately, which can cause small mean range differences between stations.

3.20 Converged T2
Shapiro delay, atmospheric delay, corner cube delay, and any bias are added on to $\rho_{12}/c=|\boldsymbol{\rho}_{12}|/c$ from equation (18) to get T2−T1, the up-leg light time, in TDB time units.

$$T2(TDB) - T1(TDB) = \frac{\rho_{12}}{c} + \delta t_{ATM} + \sum_{j} \delta t_j + \delta t_{CC} + \delta t_B \qquad (21)$$

The computation for T2−T1 is iterated until the change is <0.864 psec.

With the T2 time established, the solution parameters associated with the Moon require that partial derivatives of the range with respect to those parameters be computed. Examples of geometric parameters include retroreflector array X, Y, Z coordinates and rates, displacement Love numbers h_2 and l_2, dissipation related parameters h_2/Q_h and l_2/Q_l associated with the Love numbers (Appendix A.1), and range scale and scale rate. Geometric partials are solely generated in LPRED. Dynamical parameters are associated with the lunar orbit and orientation: the orbit and physical libration initial conditions, GM(Earth+Moon), tidal potential Love number k_2 and a tidal time lag associated with dissipation, moment of inertia combinations β=$(C–A)/B$ and γ=$(B–A)/C$, second- and third-degree gravity harmonics, and core-mantle boundary dissipation and flattening. The dynamical partials require that partials of the lunar position and Euler angles be supplied

from files. LPRED converts those partials of position and orientation into partials of range using equation (18) and the chain rule.

3.21 Down-Leg Light Time
The down-leg light-time iteration starts with an initial estimate of T3(TDB)−T2(TDB) based on observed [T3(UTC)−T1(UTC)] minus computed [T2(TDB)−T1(TDB)]. The Earth-fixed station vector at T3 includes the slow station motion and pole tide from the T1 calculation. The Earth and station vector are oriented in space with updated values at T3 for GMST(UT1), precession, and nutation. However, the small semidiurnal and diurnal corrections to UT1 and polar motion at T1 are used in the orientation.

The small tidal corrections at T1 are added on to the station vector at T3. The main solid-body tides at the station are computed and added on to the geocentric station vector. The Lorentz contraction and relativistic scale are applied. The atmospheric and Shapiro delays are computed and applied. After iteration, the analog of equation (21) gives Δt_{23}=T3(TDB)−T2(TDB).

3.22 Total Light Time
The total computed light time [T2(TDB)−T1(TDB)] + [T3(TDB)−T2(TDB)] is combined with the difference in the relativistic time transformations at the transmit and receive times [T1(TDB)−T1(TAI)] − [T3(TDB)−T3(TAI)] from eq. (5). This gives the total light time T3(TAI)−T1(TAI), which is compared with the observed value of T3(UTC)−T1(UTC) to get the observed minus computed (O–C) residual.

Many partial derivatives of range with respect to solution parameters are computed. The partial derivatives at T1, T2, and T3 are combined to get the partials for the total light time.

This completes the overview of the LPRED model for range. We continue with a list of solution parameters and possible model changes.

4. Solution Parameters
The range model is the focus of this memo, but many of the values of model parameters can be modified with solution parameters. Nominal values of most solution parameters can be input and all solution parameters Δx can be constrained with linear combinations of the form $a\Delta x=c$ or $a\Delta x_1+b\Delta x_2=c$. The following are important solution parameters that may be used with a standard LLR weighted least-squares solution.
- Station coordinates: radius, east longitude, and latitude.
- Station motion: rates up (radial), east, and north.
- Retroreflector coordinates: lunar *X, Y, Z* using a principal axis frame.
- Terrestrial Love numbers h_2 and l_2.
- Smoothed stochastic corrections for UT1 and polar motion. Corrections depend on the uncertainty in the input table values.
- Earth orientation: 2 constant angles (at J2000) and 2 rates (related to precession and obliquity rates). These angles are small rotations about two axes, one pointing toward the precessing equinox and one 90º ahead on the equator.

- Earth orienting nutations: cosine and sine coefficients for 2 axes for each of 4 nutation periods: 18.6 yr, 9.3 yr, 1 yr, and 1/2 year. The same two orientation axes are used as for the preceding orientation.
- Lunar Love numbers h_2 and l_2 and dissipation related h_2/Q_h and l_2/Q_l.
- Biases for specified stations and time spans. Overall biases between stations are typically a few cm. Bias rates can be solved for, but are not common. Infrared biases can be separate from visual wavelength biases.
- *GM* of Earth+Moon.
- Six set III parameters that specify 6 corrections to the initial condition for the lunar orbit integration. The set III parameter corrections are increments that have zero nominal values.
- Five terrestrial tidal dissipation time delays (phase shifts): 1 for zonal tides, 2 for diurnal tides, and 2 for semidiurnal tides [*Williams and Boggs*, 2016].
- Six initial conditions for the integration of the orientation of the Moon's crust and mantle. Three are Euler angles and 3 are angular rates about the X, Y, and Z principal axes.
- Three angular rates about the lunar X, Y, and Z axes for the fluid core initial conditions.
- Lunar Love number k_2.
- Time delay τ_M associated with k_2 and tidal dissipation. The lunar tide is evaluated at time $t-\tau_M$ for the dynamical model.
- An energy dissipation parameter for relative motion at the lunar core-mantle boundary [*Williams et al.*, 2001].
- A flattening parameter for the lunar core-mantle boundary.
- Lunar moment of inertia expressions $\beta=(C-A)/B$ and $\gamma=(B-A)/C$ plus J_2 and 7 third-degree gravity harmonic coefficients. *A*, *B*, and *C* are the principal moments of inertia about the three principal axes, $A<B<C$.
- Cosine and sine coefficients for physical libration parameters associated with dissipation at 206 d = 7 months, 1 yr, 1095 d = 3 yr, and 2190 d = 6 yr (and sometimes 1 month) [*Williams and Boggs*, 2015]. Additional cosine and sine coefficients are available at 1306 d and 1643 d. The latter selections are empirical, but based on known periods [*Rambaux and Williams*, 2011].
- Lunar orbit extra eccentricity rate.
- Vertical thermal expansion of Apollo and Lunokhod structures.

When joint solutions are made to produce a lunar and planetary ephemeris [*Williams et al.*, 2013; *Folkner et al.*, 2014], additional solution parameters are needed.
- The mass ratio, Earth/Moon.
- Set III corrections to the initial conditions of the planets from Mercury to Jupiter.
- Solar J_2.

Solutions for gravitational physics parameters [*Williams et al.*, 2004, 2009] may include:
- PPN β and γ.
- Equivalence principle gravitational/inertial mass ratio for Earth.
- Cos *D* and sin *D* coefficients in range.

- Rate of change of the gravitational constant G, as $(dG/dt)/G$.
- Rate of change of solar mass, $(dM_S/dt)/M_S$, from J2000.
- A factor to test geodetic precession rate.
- Range scale factor and rate. The scale rate was used to determine a limit for any rate of change of the speed of light [*Williams et al.*, 2014a].

Other programs solve the least-squares equations and display post-fit residuals.

5. Toward an Improved Model

For the LLR normal points, there is a spread of range accuracies that depends on the laser pulse width, the timing accuracy for a single detected photon, and the number of photons in each normal point. During the first 25 yr shown in Figure 1, the data noise was greater than the modeling error. During the last one or two decades, there have been ranges that are more accurate than our fits. Can future modeling improvements reduce the residuals further?

The LLR model for terrestrial orientation from nutation and terms associated with the equation of equinox could be modernized. We note that the Earth's J_2 rate is changing [*Cheng et al.*, 2013]. A solution parameter that alters the acceleration of precession may be useful.

The atmospheric delay is meters in size. Very good accuracy is required for the atmospheric model. As the IERS Conventions notes, horizontal pressure gradients are a possible source of systematic error during off-zenith ranging sessions. The relevant horizontal scale for pressure gradients is set by the scale height, ~8.5 km, times the cotangent of elevation. Pressure gradients are not presently provided with the data.

Does the pressure dependence of the atmospheric delay need a separate factor for each station? We note that the differences in the mean pressure at the three McDonald sites do not match their height differences.

Is there significant thermal expansion and contraction of a telescope and its mount or is there a thermal influence on the delay calibration? The rms temperature variations in Table 4 are modest and the thermal effect on few-meter sized structures appears small.

Fits over <10 yr of data have less rms scatter than the same spans with fits over the full 50 yr span. Range residuals show small physical libration signatures. Spectra of residuals indicate that much of the libration noise is long period (≥ 2 yr). Some long-period adjustment of physical librations should tighten the rms scatter.

The terrestrial model may have several millimeters of rms noise that might be improved. The lunar model has systematic effects in orientation that are not well understood. Possible improvements to the dynamical model are not part of this memo.

6. Summary

This overview of the data analysis program LPRED describes the LLR data in section 2 and the model for terrestrial, orbital, and lunar effects that affect the range is in section 3. Common solution parameters are listed in section 4 and modeling concerns are discussed in section 5.

Appendices

A1. Monthly Tidal Variations on Moon

The physical librations are sensitive to multiple periods and the main (elastic-like) tidal displacements reach 0.1 m (Fig. 4), but there are also small phase shifts in the displacements due to tidal dissipation. The largest of these phase-shifted monthly tidal displacements on the Moon occur at the anomalistic (l) month (27.555 d) and nodical (F) month (27.212 d). The cosine and sine coefficients are given in Table A.1. DE440 used model values of $h_2/Q_h = 1.0 \times 10^{-3}$ and $l_2/Q_l = 3.0 \times 10^{-5}$. These should be considered as approximate and measurements would be valuable. With the model h_2/Q_h, the largest vertical displacements are 2.2 mm for Apollo 11 and 14. With the model l_2/Q_l, the largest horizontal displacements are a few tenths of a millimeter.

Table A.1. The largest monthly tidal displacements. Multiply argument l terms by h_2/Q_h and F terms by l_2/Q_l.

Reflector	Arg	Up cos m	Up sin m	East cos m	East sin m	North sos m	North sin m
Apollo 11	l	-1.540	1.618	-2.924	-2.282	0.037	-0.064
Apollo 11	F	0.050	0.000	-0.022	0.000	4.158	-0.010
Apollo 14	l	1.229	1.800	-3.464	1.834	0.156	0.361
Apollo 14	F	-0.273	0.000	-0.086	0.002	4.289	0.008
Apollo 15	l	-0.204	1.484	-3.790	-0.326	0.206	-2.494
Apollo 15	F	1.790	-0.001	-0.126	-0.011	2.767	-0.001
Lunokhod 1	l	1.232	0.240	-1.119	2.338	-1.962	-2.048
Lunokhod 1	F	1.806	0.000	1.614	-0.013	0.856	0.003
Lunokhod 2	l	-1.511	0.843	-1.828	-2.491	1.456	-1.841
Lunokhod 2	F	1.527	0.000	-1.015	-0.010	2.411	-0.008

A2. Constant Tidal Displacements on Moon

Table A.2 gives the constant tides from Earth and Sun, but not spin or 3rd degree tides, for the DE440 Love numbers $h_2 = 0.0423$ and $l_2 = 0.0107$.

Table A.2. Constant tides from Earth and Sun for the DE440 Love numbers $h_2 = 0.0423$ and $l_2 = 0.0107$.

Reflector	X mm	Y mm	Z mm	Up mm	East mm	North mm
Apollo 11	441.2	27.0	0.8	415.5	-150.8	-4.2
Apollo 14	482.6	-28.2	-5.9	468.2	118.2	23.8
Apollo 15	416.6	2.9	22.5	383.3	-23.3	-163.2
Lunokhod 1	197.5	47.5	-66.0	64.5	152.3	-135.2
Lunokhod 2	294.8	-14.4	-14.0	214.9	-163.8	-119.7

Abbreviations

BCRS Barycentric Celestial Reference System, formerly BRS. Compatible with TCB.
FCN Free Core Nutation. An ~14 month variation due to the fluid core.
GCRS Geocentric Celestial Reference System, formerly GRS. Compatible with TCG.
GMST Greenwich Mean Sidereal Time. The rotation of the Earth with the prime
meridian referred to the slowly precessing equinox.
GST Greenwich Sidereal Time. The rotation of the Earth with the prime meridian
referred to the precessing and nutating equinox.
IAU International Astronomical Union.
ICRF International Celestial Reference Frame.
IERS International Earth Rotation Service.
ILRS International Laser Ranging Service.
ITRF International Terrestrial Reference Frame.
ITRS International Terrestrial Reference System.
JD Julian day.
LLR Lunar Laser Ranging.
MJD Modified Julian day, JD−2400000.5.
PPN Parameterized Post-Newtonian. A gravitational formulation more general than
General Relativity.
SLR Satellite Laser Ranging.
TAI International Atomic Time. A continuous time scale for the Earth's surface.
TCB Barycentric Coordinate Time. A solar system barycentric coordinate time.
TCG Geocentric Coordinate Time.
TDB Barycentric Dynamical Time. A solar system coordinate time used for JPL lunar
and planetary ephemerides.
TT Terrestrial Time. TT = TAI + 32.184 sec.
UTC Universal Time Coordinated. This time, used for recording observations,
experiences occasional leap seconds with respect to TAI.
UT1 Universal Time. This representation uses the Earth's rotation as a clock. Due to
variations in rotation rate, it is not a uniform time scale.

Acknowledgments

References

Cheng, M., B. D. Tapley, and J. C. Ries (2013), Deceleration in the Earth's oblateness, *J. Geophys. Res. Solid Earth*, *118*, 740–747, doi:10.1002/jgrb50058.

Dickey, J. O., P. L. Bender, J. E. Faller, X X Newhall, R. L. Ricklefs, J. G. Ries, P. J. Shelus, C. Veillet, A. L. Whipple, J. R. Wiant, J. G. Williams, and C. F. Yoder (1994), Lunar Laser Ranging: A continuing legacy of the Apollo program, *Science*, *265*, 482–490, doi:10.1126/science.265.5171.482.

Fairhead, L., and P. Bretagnon (1990), An analytical formula for the time transformation TB−TT, *Astron. Astrophys*., *229*, 240–247.

Folkner, W. M., J. G. Williams, D. H. Boggs, R. S. Park, and P. Kuchynka (2014), The planetary and lunar ephemerides DE430 and DE431, *Interplanetary Network Progress Rep. 42–196*, Jet Propul. Lab., Pasadena, Calif., 15 Feb. 2014, http://ipnpr.jpl.nasa.gov/progress_report/42-196/196C.pdf .

Harada, W., and T. Fukushima (2003), Harmonic decomposition of the time ephemeris TE405, *Astron. J*., *126*, 2557–2561, doi:10.1086/378909.

Heraeus (2011), Quartz glass for optics, data and properties, https://www.heraeus.com/media/media/hca/doc_hca/products_and_solutions_8/optics/Data_and_Properties_Optics_fused_silica_EN.pdf .

Hilton, J. L., N Capitaine, J. Chapront, J. M. Ferrandiz, A. Fienga, T. Fukushima, J. Getino, P. Mathews, J.-L. Simon, M. Soffel, J. Vondrak, P. Wallace, and J. Williams (2006), Report of the International Astronomical Union division I Working Group on precession and the ecliptic, *Celestial Mech. and Dyn. Astron., 94*(3), 351–367, doi: 10.1007/s10569-006-0001-2.

Moyer, T. D. (1981a), Transformation from proper time on Earth to coordinate time in solar system barycentric space-time frame of reference, Part 1, *Celes. Mech*., *23*, 33–56, doi:10.1007/BF01228543.

Moyer, T. D. (1981b), Transformation from proper time on Earth to coordinate time in solar system barycentric space-time frame of reference, Part 2, *Celes. Mech.*, *23*, 57–68, doi:10.1007/BF01228544.

Moyer, T. D. (2000), Formulation for observed and computed values of Deep Space Network data types for navigation, Deep Space Communications and Navigation Series, JPL Publication 00-7.

Müller, J., T. W. Murphy, Jr., U. Schreiber, P. J. Shelus, J.-M. Torre, J. G. Williams, D. H. Boggs, S. Bouquillon, A. Bourgoin, and F. Hofmann (2019), Lunar laser ranging – a tool for general relativity, lunar geophysics and earth science, J. Geod., 93 (issue 11), 2195-2210, doi:10.1007/s00190-019-01296-0 . http://link.springer.com/article/10.1007/s00190-019-01296-0 http://www.researchgate.net/publication/234081755_Lunar_Laser_Ranging__A_Tool_for_General_Relativity_Lunar_Geophysics_and_Earth_Science

Murphy, T. W. Jr, E. G. Adelberger, J. B. R. Battat, C. D. Hoyle, N. H. Johnson, R. J. McMillan, E. L. Michelson, C. W. Stubbs, and H. E. Swanson (2011), Laser ranging to the lost Lunokhod 1 reflector, *Icarus*, *211*, 1103–1108, doi:10.1016/j.icarus.2010.11.010.

Murphy, T. W. (2013), Lunar laser ranging: the millimeter challenge, *Rep. Prog. Phys.*, *76*, 076901, doi:10.1088/0034-4885/76/7/076901.

Park, R. S., W. M. Folkner, J. G. Williams, and D. H. Boggs (2020), The JPL Planetary and Lunar Ephemerides DE 440 and DE441 (2020), accepted by *Astron. J.*

Pearlman, M.R., J. J. Degnan, and J. M. Bosworth (2002), The international laser ranging service, *Adv. Space Res.*, *30*(2), 135–143, doi:10.1016/S0273-1177(02)00277-6.

Petit, G., and B. Luzum (eds.) (2010), IERS Conventions (2010), IERS Tech. Note 36, Verlag des Bundesamts für Kartographie und Geodäsie, Frankfurt am Main 2010, pp. 179, http://www.iers.org/TN36/.

Shapiro, I. I., (1964), Fourth test of general relativity, *Phys. Rev. Lett.*, *13*, 789–791.

Standish, E. M., and J. G. Williams (2013), Orbital ephemerides of the Sun, Moon, and planets, in *Explanatory Supplement to the Astronomical Almanac*, 3rd ed., edited by. S. Urban and P. K. Seidelmann, pp. 305–345, University Science Books, Mill Valley, Calif., http://iau-comm4.jpl.nasa.gov/XSChap8.pdf .

Williams, J. G., D. H. Boggs, C. F. Yoder, J. T. Ratcliff, and J. O. Dickey (2001), Lunar rotational dissipation in solid body and molten core, *J. Geophys. Res.*, *106*, 27,933–27,968, doi:10.1029/2000JE001396.

Williams, J. G., S. G. Turyshev, and D. H. Boggs (2004), Progress in lunar laser ranging tests of relativistic gravity, *Phys. Rev. Lett.*, *93*, 261101, doi:10.1103/PhysRevLett.93.261101, arXiv:gr-qc/0411113

Williams, J. G., S. G. Turyshev, and D. H. Boggs (2009), Lunar Laser Ranging Tests of the Equivalence Principle with the Earth and Moon, *International Journal of Modern Physics D*, *18*(7), 1129–1175, doi:10.1142/S021827180901500X.

Williams, J. G., D. H. Boggs, and W. M. Folkner (2013), DE430 Lunar Orbit, Physical Librations, and Surface Coordinates, IOM 335-JW,DB,WF-20130722-016, July 22, 2013, Jet Propul. Lab., Pasadena, Calif., http://naif.jpl.nasa.gov/pub/naif/generic_kernels/spk/planets/de430_moon_coord.pdf .

Williams, J. G., S. G. Turyshev, and D. H. Boggs (2014a), The past and present Earth-Moon system: the speed of light stays steady as tides evolve, Planetary Science, 3, 2, doi:10.1186/s13535-014-0002-5, http://www.planetary-science.com/content/3/1/2 .

Williams, James G., Alexander S. Konopliv, Dale H. Boggs, Ryan S. Park, Dah-Ning Yuan, Frank G. Lemoine, Sander Goossens, Erwan Mazarico, Francis Nimmo, Renee C. Weber, Sami W. Asmar, H. Jay Melosh, Gregory A. Neumann, Roger J. Phillips, David E. Smith, Sean C. Solomon, Michael M. Watkins, Mark A. Wieczorek, Jeffrey C. Andrews-Hanna, James W. Head, Walter S. Kiefer, Isamu Matsuyama, Patrick J. McGovern, G. Jeffrey Taylor, and Maria T. Zuber (2014b), Lunar interior properties from the GRAIL mission, *J. Geophys. Res. Planets*, *119*, 1546–1578, doi:10.1002/2013JE004559.

Williams, J. G., and D. H. Boggs (2015), Tides on the Moon: Theory and determination of dissipation, *J. Geophys. Res. Planets*, *120*, 689–724, doi:10.1002/2014JE004755.

Williams, J. G., and D. H. Boggs (2015), The JPL lunar laser range model, JPL IOM 335-JGW,DHB-20150701-32, July 1, 2015.

Williams, James G. and Dale H. Boggs (2016), Secular tidal changes in lunar orbit and Earth rotation, *Celest. Mech. and Dynamical Astron.*, 126, 89–129, doi:10.1007/s10569-016-9702-3.

Williams, J. G., D. H. Boggs, R. Park, and W. M. Folkner (2020), DE440 Lunar Orbit, Physical Librations, and Surface Coordinates, IOM 335-JW,DB,RP,WF-in preparation, December 2020, Jet Propul. Lab., Pasadena, Calif.

Wu, X., J. Ray, and T. van Dam (2012), Geocenter motion and its geodetic and geophysical implications, *J. Geodyn.*, *58*, 44–61, doi:10.1016/j.jog.2012.01.007.

Wu, X., J. Kusche, and F. W. Landerer (2017), A new unified approach to determining geocentre motion using space geodetic and GRACE gravity data, *Geophys. J. Int.*, 209, 1398–1402, doi:10.1093/gji/ggx086.

Yagudina, E. I., D. A. Pavlov, V. N. Tryapitsyn, and V. V. Rumyantsev (2018), Processing and analysis or lunar laser ranging observations in Crimea in1974–1984, poster B30 at 21st International Workshop on Laser Ranging, Canberra, Australia, November 5–9, 2018.